

5.3 Investigation of Fog and Low Clouds Associated with a Coastally Trapped Disturbance

William T. Thompson* and Stephen D. Burk
Naval Research Laboratory

Monterey, CA

1. INTRODUCTION

One of the most distinctive features of coastally trapped disturbances (CTD's) is the tongue of fog and low clouds propagating poleward along the west coast of continents against the typical coast-parallel equatorward flow. In this study, characteristics of the fog and low clouds observed in conjunction with a CTD event on 15-16 June 2000 are investigated. In particular, we examine the relative importance of radiation, cloud microphysical processes, advection, entrainment, and surface fluxes to the fog and cloud layer associated with the CTD. The synoptic setting in which the CTD was observed is also documented. A simulation of the event is produced using the Naval Research Laboratory's nonhydrostatic Coupled Ocean/Atmosphere Mesoscale Prediction System (COAMPS™; COAMPS is a trademark of the Naval Research Laboratory). Propagation of the wind shift and cloud tongue and the extent of fog and low clouds in the model results are compared with coastal buoy data and satellite imagery. We also investigate the thermodynamics and integral energetic properties of the fog and low cloud layers and perform several sensitivity studies.

2. RESULTS

2.1 Model Description

The COAMPS™ model is a nonhydrostatic mesoscale model, using multiple nests having different horizontal resolution. It features a full suite of physical parameterizations, including schemes for radiation, cloud microphysics, and turbulence. Time-dependent lateral boundary conditions are

obtained from the Navy global model (NOGAPS) and applied to the boundaries of the outermost nest. Lateral boundary conditions on inner nests are supplied by outer nests; if N is the innermost nest and 1 is the outermost, boundary conditions on nest m are supplied by nest $m - 1$ (where $m \geq 2$). Data assimilation is accomplished using a scheme which, in the absence of observational data, retains horizontal and vertical structure developed in the previous forecast in the initial conditions of a subsequent forecast. Where observational data are available, these data are incorporated into the initial conditions using an increment formed between the observational analysis and the previous forecast. The model is described in more detail by Hodur et al. (2002).

In the present study, the model is run in a triply-nested mode with horizontal resolutions of 45 km, 15 km, and 5 km. The innermost nest consists of 181X181 grid points extending from 31° N to 39° N and from 117° W to 126° W (Figure 1). In the vertical, 45 levels are used from the surface to ~ 30 Km with 10 m resolution near the surface.

2.2 Mesoscale Evolution

Shown in Figure 2a is the region over which the COAMPS™ cloud liquid water mixing ratio at 10 m elevation exceeds 0.01g/Kg (which we term the "fog footprint") at 1700 LT 15 June. Experience with the model shows that this rather low threshold value corresponds to the lowest liquid water content at which visibility is reduced due to fog. The fog extends from just south of Pt. Arena to the northern portion of the Southern California Bight and offshore to near

• Corresponding Author: William T. Thompson
Naval Research Laboratory, Monterey
CA. thompson@nrlmry.navy.mil

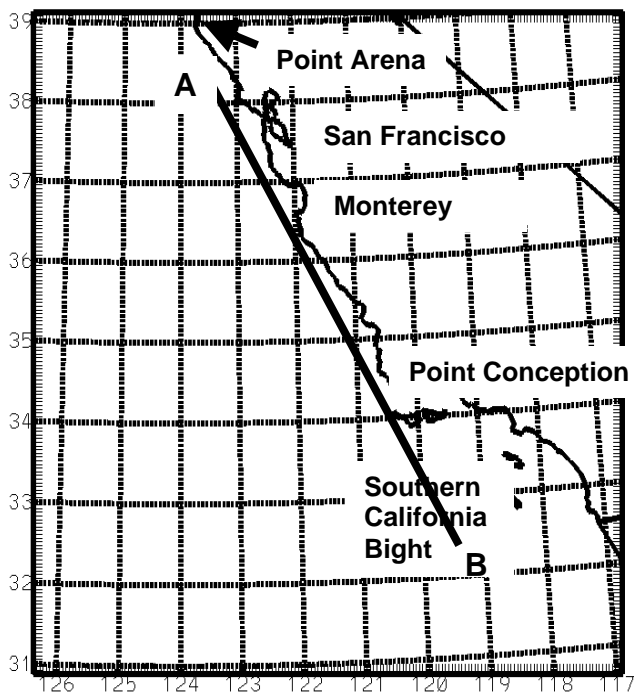


Figure 1. 9 km nest domain.

surface to form low clouds which extend nearly to the southern boundary of the domain east of 122°W and to the western boundary of the domain north of 32°N . The extent of low clouds is shown in Figure 2b, which depicts the 0.01 g/Kg isosurface of cloud liquid water. In this depiction, all areas in which cloud water is nonzero are shown with no regard to elevation.

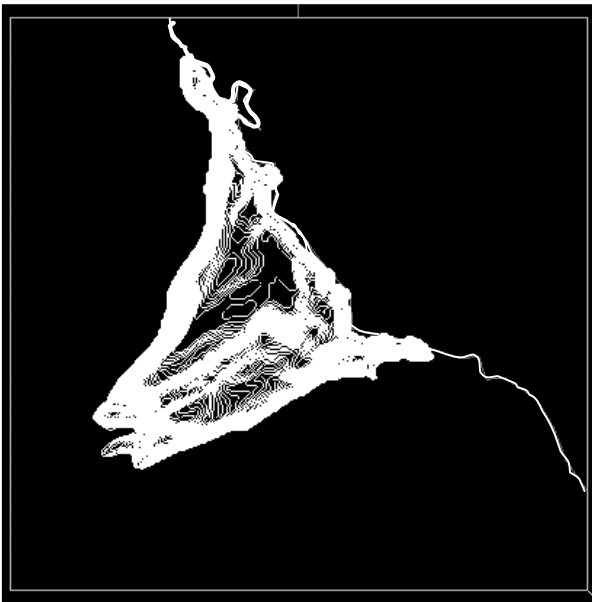


Figure 2a. Cloud liquid water at 10 m elevation.

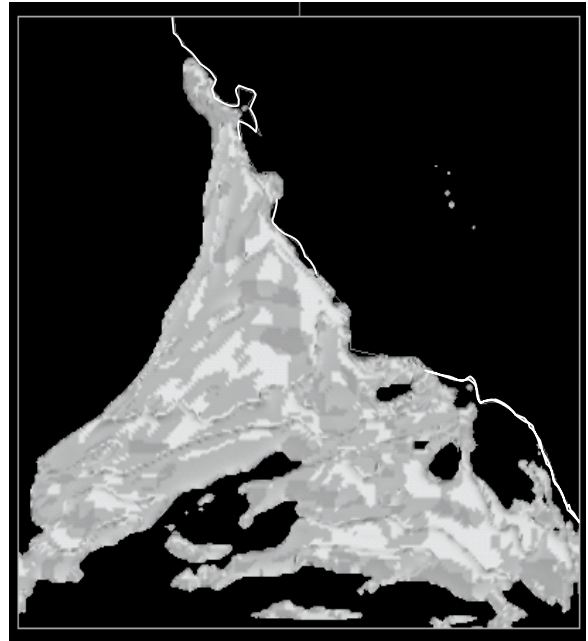


Figure 2b. Cloud liquid water isosurface (0.01 gm Kg^{-1}).

Thus, this figure shows the areal extent of both fog and low clouds. Comparison of Figure 2a to Figure 2b shows extensive low cloudiness to the south and throughout the Southern California Bight. The depiction in Figure 2b) is similar to a satellite image. Comparison of Figure 2b with the satellite image in Figure 3 shows reasonable agreement, although the fog tongue in the satellite is $\sim 40 \text{ km}$ further north and there is no eddy formation indicated in the model results (the immediate Southern California Coastal zone is clear in both the model results and satellite). In addition, some of the clearing to the south in the model results does not verify (although Figure 2 extends further to the west that does the satellite image).

Figure 4a displays a cross section of potential temperature (contours) and cloud liquid water (shaded) in the plane A-B of Figure 1 extending from the surface to 1500 m valid 0500 LT 15 June 2000 while Figure 4b shows the same depiction valid 1700 LT 15 June. In the northerly flow north of the wind shift line, strong stable stratification extends to the surface, while a very shallow mixed layer is forming between the wind shift line and the leading edge of the fog (Figure 4a). Within the fog, the boundary layer is well-mixed and deepens to the south due to the combined effects of cloud top radiative cooling and upward surface heat flux. The deeper boundary

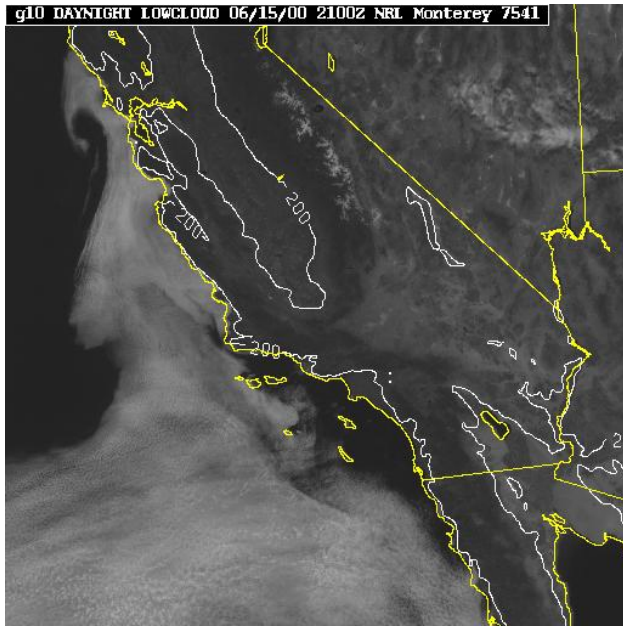


Figure 3. Satellite image valid 1400 LT 15 June 2000.

layer is more turbulent and enhances entrainment of warm, dry air and the lifting condensation level (LCL) lifts off the surface as the cloud base rises to form low clouds. At the southern end of the cross section, the boundary layer is 450 m deep. At the point at which the cloud base lifts away from the surface, the fog layer is ~300 m deep while at the southern end of the cross section, the cloud layer is only 150 m deep (Figure 4b).

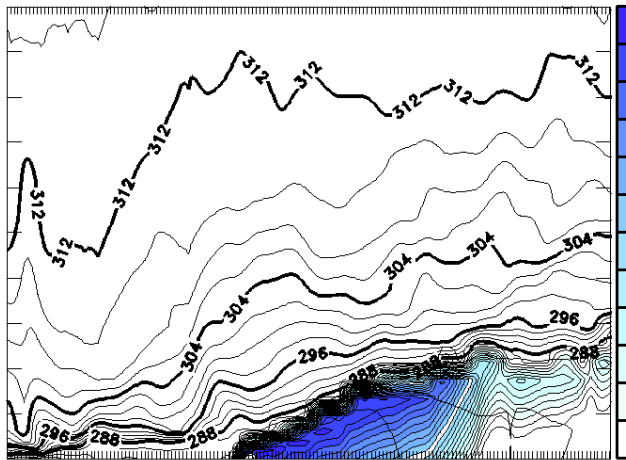


Figure 4a. Cross section of potential temperature (K) and cloud liquid water (shaded) valid 0500 LT 15 June.

2.3 Fog and Cloud Layer Moist Thermodynamic Processes

The surface latent and sensible heat fluxes are, not surprisingly, tightly coupled with the fog. In particular, the transition from upward to downward sensible heat flux (the 0 contour) is co-located with the northern boundary of the fog footprint with downward fluxes to the north and upward fluxes to the south. The northern boundary is also co-located with a relative minimum in latent heat flux. Examination of the Bowen Ratio (the ratio of sensible to latent heat flux) shows an interesting result; the 0.5 contour of Bowen Ratio closely corresponds to the fog footprint boundary. The conclusion drawn from this result is that this critical value near 0.5 arises from the relationship between variations in mixing ratio and temperature change imposed by the saturated condition. South of the fog footprint boundary, the Bowen Ratio is less than 0.5 while, to the north, the value is negative (the sensible heat flux is negative, while the latent heat flux remains upward except in small, isolated regions).

Although the Bowen ratio delineates the fog boundary well, it provides little information on the relative roles of sensible and latent heat flux energetic contributions to the cloud layer dynamics. The Bowen ratio cannot be expected to represent the role of turbulent fluxes throughout the

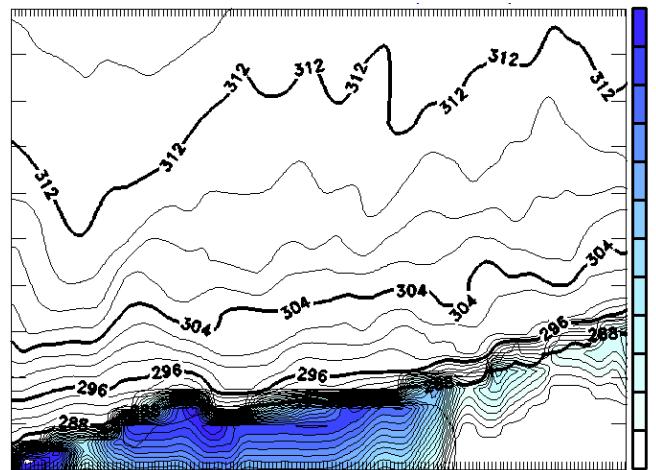


Figure 4b. As in Fig. 4a but valid 1700 LT 15 June.

cloud layer, due to the influence of other important processes such as entrainment, cloud-top radiative cooling, and evaporative cooling (Lewellen et al. 1996). In order to characterize the contribution of the integrated effect of latent heat release to the integral of total buoyancy flux generation, we define the total virtual buoyancy flux as

$$\langle w'\theta'_v \rangle = \beta_T \langle w'\theta'_l \rangle + \beta_l \langle w'q'_l \rangle + \beta_w \langle w'q'_w \rangle \quad (1)$$

where $\langle w'q'_w \rangle$ is the turbulent flux of total moisture and $\langle w'q'_l \rangle$ is the turbulent liquid water flux. In the physics option of COAMPS™ used here, liquid water flux may be written as:

$$\langle w'q'_l \rangle = R'(a \langle w'q'_w \rangle - b \langle w'\theta'_l \rangle) \quad (2)$$

where a and b are functions of saturation mixing ratio, pressure, and temperature and where $\langle w'\theta'_l \rangle$ is the turbulent flux of liquid water potential temperature, R' is a function of the statistical cloud fraction R (obtained from a cloud fraction scheme using a Gaussian pdf), and the values of β_T , β_l , and β_w are given in Yamada (1978) and Yamada and Mellor (1979).

The results show that, over most of the region of the fog footprint (northern~2/3), the liquid water flux is negative due to the dominance of cloud top radiative cooling over entrainment and evaporation. Negative values of liquid water flux can also be inferred in the investigation of Lewellen and Lewellen (1998; their Figure 13 and personal communication). When the liquid water flux is negative, downward perturbations in vertical velocity are associated with positive perturbations in liquid water due to strong radiative cooling and condensation near the top of the fog. Equation (2) above can be solved for $\langle w'q'_w \rangle$ to give

$$\langle w'q'_w \rangle = \frac{1}{a} (\langle w'q'_l \rangle + b \langle w'\theta'_l \rangle) \quad (3)$$

(assuming that $R'=1$) where a and b are given in equation (3) above. With some fur-

ther re-arrangement, a new expression for virtual buoyancy flux can be obtained:

$$\langle w'\theta'_v \rangle = \left(\beta_T + \frac{\beta_w b}{a} \right) \langle w'\theta'_l \rangle + \left(\beta_l + \frac{\beta_w}{a} \right) \langle w'q'_l \rangle \quad (4)$$

(Yamada and Mellor 1979) (the coefficients on the fluxes are always positive). Thus, from equation (4), negative liquid water flux reduces total virtual buoyancy flux. Over the northern portion of the fog footprint, virtual buoyancy flux is reduced due to negative liquid water flux, reducing buoyant production of TKE and entrainment. Further to the south, the boundary layer is deeper, TKE is greater, and entrainment is enhanced which leads to the evaporation of liquid water near cloud top. Ultimately, buoyancy generation due to evaporation exceeds buoyancy consumption due to condensation and the liquid water flux becomes positive which leads to a further increase in virtual buoyancy flux. Still further to the south, entrainment of dry air results in the LCL lifting off the surface as the cloud base rises to form a low cloud layer.

The importance of radiative cooling in forcing negative values in the liquid water flux was established in an experiment in which radiative cooling was eliminated; in this case, liquid water flux was everywhere positive.

In an effort to gauge the impact of the negative liquid water flux on the dynamics, several sensitivity studies were conducted. The results indicated that changes in the sign of the liquid water flux are of secondary importance. The primary process determining the distribution of boundary layer depth and the extent of fog and low clouds is the southward increase in buoyancy generation due to surface fluxes and in-cloud process, as noted in the previous section.

To examine the distribution of the fluxes as the LCL lifts off the surface, profiles of the thermodynamic fluxes are plotted at several times at a location at the edge of the fog footprint (33.3°N, 122°W). At this location, the fog lifts off the surface at hour 9. Profiles at hours 6, 9, and 12 are shown in Figure 5a-c. In figure 5, the profiles are identified by letter; A is the total water flux term (term 3 on the RHS of equation 1), B is the liquid water flux term (term 2 on the RHS of equation 1), C is the liquid water potential

temperature flux term (term 1 on the RHS of equation 1), and D is the virtual buoyancy flux (the LHS of equation 1); thus, A, B, and C sum to D. The boundary layer depth is 260 m at hour 6 and ~350 m at hours 9 and 12. Note that the distribution of the liquid water flux is such that the integral of this quantity is negative at hour 6 (Fig 5a) and positive at hours 9 and 12 (Fig 5b, c) and, moreover, that the magnitude of the negative peak decreases monotonically from hour 6 to zero at hour 12. Thus, the impact of condensation associated with downdrafts on liquid water flux decreases with time as the fog layer begins to rise to form low clouds; i.e., condensation and release of latent heat become more associated with updrafts rather than with downdrafts.

The liquid water flux (B) is positive in the upper portion of the cloud. This is the result of entrainment of warm, dry air (as indicated by the liquid water potential temperature flux (C)) and evaporation of cloud water. Radiative flux divergence at cloud top results in positive term C and negative liquid water flux due to condensation associated with downdrafts as discussed above. Note, however, that the effect of radiative cooling on the fluxes is seen in the lower portion of the cloud in spite of the fact that the cooling takes place in the upper few 10's of meters of the cloud. Destabilization of the mixed layer by radiative cooling results in vigorous turbulent mixing.

From the vertical distribution of the fluxes in Figure 5a-c, it is evident that significant entrainment occurs at hour 9 as the fog lifts away from the surface. The magnitude of the negative virtual buoyancy flux in the cloud layer at this time is significantly larger (by nearly a factor of three) than at the other times shown. Thus, the magnitude of the liquid water potential temperature flux and the liquid water flux, i.e., entrainment warming/drying and evaporation of cloud water, increase significantly as the cloud base lifts off the surface to form low clouds.

3. The Role of Surface Fluxes in CTD Fog/Cloud Evolution

As the CTD propagates to the north along the coast, the wind shift from northerly to southerly is followed after ~2-3 h by fog and low clouds. In this study we find evidence that the timing difference between arrival of the CTD's wind shift and the arrival

of the fog is central to the evolution of the cloud liquid water field. Within the zone between the wind shift and the leading edge of the fog, strong near surface convergence begins to lift and cool the strongly stratified air adjacent to the surface (Figure 6). If the wind shift line and preconditioning region propagate at a phase speed, c , that exceeds the mean southerly wind in this region, then the cloud tongue will not simply advect along but rather advance faster than the mean cloud layer wind. Viewed in a Lagrangian reference frame that is propagating with phase speed c , the preconditioning region locally takes on the *appearance* of an internal boundary layer (IBL) that grows downwind with fetch.

In a sensitivity study in which both latent and sensible surface heat fluxes are removed, results show that there is extensive compensation between latent and sensible heating as the results are quite similar to the control. The results of this simulation call into question the commonly accepted hypotheses that the cold SST along the coast is responsible for fog and cloud formation. Southerly flow over progressively cooler SST leads to cooling resulting from downward surface sensible heat flux. Were this the correct hypothesis for fog and cloud formation in this CTD event, removing the surface fluxes (as is done in this simulation) should dramatically change the cloud water field. However, in this simulation, the cloud field is largely unchanged, indicating that the cool SST is not primarily responsible for fog and cloud formation. Thus, the processes occurring in the zone between the wind shift and the fog edge take on greater significance.

ACKNOWLEDGEMENTS: This research was supported by the Office of Naval Research Program Element 0601153N.

REFERENCES

- Hodur, R. M. et al., 2002. *Oceanography*, **15**, 88-89.
- Lewellen, D. C. and W. S. Lewellen, 1998. *J. Atmos. Sci.*, **55**, 2645-2665.
- Lewellen, D. C., W. S. Lewellen, and S. Yoh, 1996. *J Atmos Sci.*, **53**, 175-187.
- Yamada, T., 1978. Argonne National Laboratory Report ANL/RER-78-1, Argonne, IL. 67 pp.
- Yamada, T. and G. L. Mellor, 1979. *Quart. J. Roy. Meteor. Soc.*, **105**, 915-944.

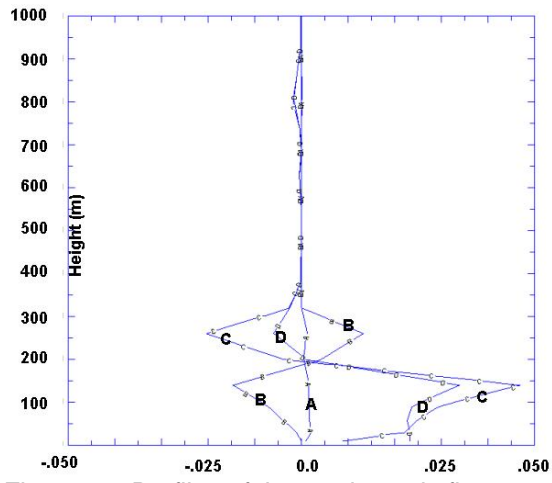


Figure 5a. Profiles of thermodynamic fluxes.

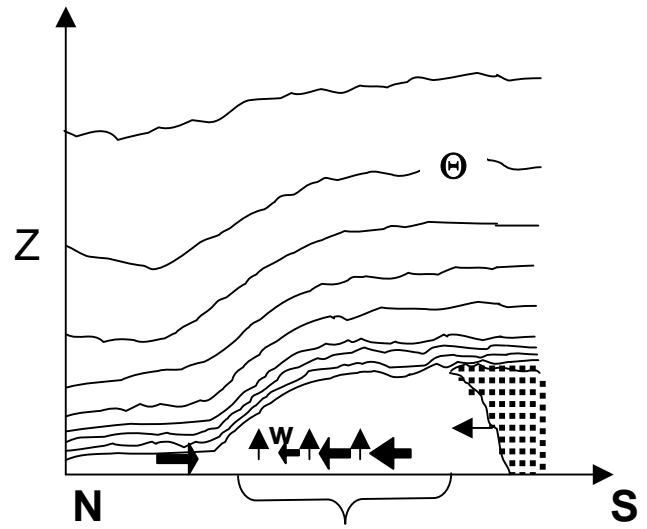


Figure 6. Propagating Zone of Convergence & Lifting Creates Preconditioning Region.

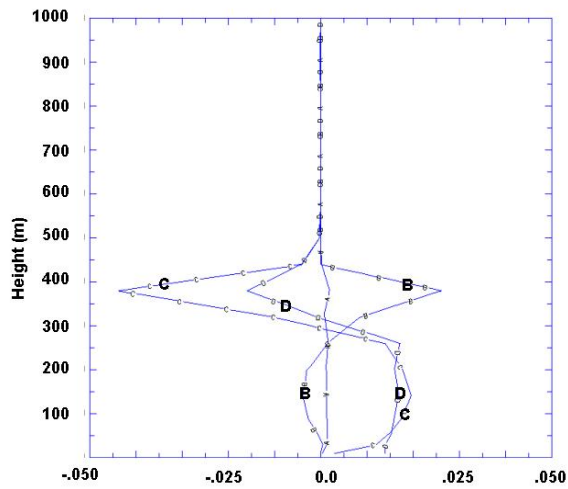


Figure 5b.

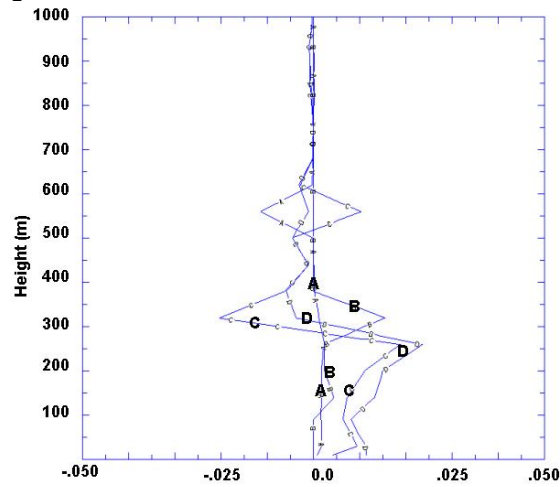


Figure 5c.